Engineering Fracture Mechanics xxx (xxxx) xxx

Contents lists available at ScienceDirect

Engineering Fracture Mechanics

journal homepage: www.elsevier.com/locate/engfracmech

A phase field solution for modelling hyperelastic material and hydrogel fracture in ABAQUS

Shoujing Zheng [1], Rong Huang [1], Ruijie Lin, Zishun Liu [*]

International Center for Applied Mechanics, State Key Laboratory for Strength and Vibration of Mechanical Structures, Xi'an Jiaotong University, Xi'an 710049, People's Republic of China

ARTICLE INFO

Keywords:
Phase field fracture
Finite element implementation
Hyperelastic material
Hydrogel

ABSTRACT

The phase field fracture model is attracting significant interest. To model fracture in hyperelastic material and hydrogel, we have implemented a robust two- and three-dimensional phase field method in the commercial finite element code ABAQUS/Standard. The method is based on the rate-independent variational principle of diffuse fracture and also exploits the analogy between the phase field evolution law and the heat transfer equation, enabling the use of Abaqus' in-built features and sparing the need for defining user elements. The framework is shown to accommodate both staggered and monolithic solution schemes. The approach can properly simulate the fracture for both hyperelastic material and hydrogel under different boundary conditions. Several examples are provided to demonstrate the robustness of the method. The provided source codes and the tutorials make it easy for practicing engineers and scientists to model crack propagation in hyperelastic and gel materials.

1. Introduction

Many hyperelastic materials show great potential in the applications, and many elastomer polymer, hydrogels and other polymer materials are modeled by hyperelastic materials. The superiority of the hyperelastic materials can be found in properties such as high stretchability [1], reversible swelling [2], flexibility [3], biocompatibility [4], and toughness [5]. Due to these extraordinary advantages, hyperelastic materials have been widely applied in drug delivery [6], tissue engineering [7], actuators [8], and so on.

With the wide engineering applications of hyperelastic materials, it is imperative to study the fracture mechanisms due to crack initiation and propagation in hyperelastic materials. Many researchers have proposed different simulation methods to investigate the fracture phenomenon of hyperelastic materials. A scaling theory that accounts for the synergistic effects of intrinsic fracture energies and dissipation on the toughening of soft materials has been developed [9,10]. Several finite-element models have been developed to simulate the adhesion fracture process of a hydrogel sheet from a rigid substrate with a layer of cohesive elements [11–13]. However, these simulations are based on the classical theory of fracture mechanics and therefore highly depends on the preset fracture propagation path.

Among many theories proposed to predict the fracture phenomenon, the phase field model spearheaded by Miehe et al. [14–17] has attracted the interest of many research groups [18–22] in recent years. The phase field model is essentially a thermodynamically consistent framework for the modeling of crack propagation, which concerns in particular the introduction of a crack surface density

* Corresponding author.
E-mail address: zishunliu@mail.xjtu.edu.cn (Z. Liu).
[1] These authors contributed equally to this work.

https://doi.org/10.1016/j.engfracmech.2022.108894
Received 14 July 2022; Received in revised form 12 September 2022; Accepted 17 October 2022
Available online 22 October 2022

function depending on a length scale. The commercial finite element software ABAQUS has received particular attention in the phase field fracture community, and vast literature have emerged on the implementation of the phase field fracture method on this commercial software [23–25]. Specifically, Molnár and Gravouil [26] have successfully achieved an ABAQUS User-defined Element subroutine (UEL) implementation of a robust staggered phase field solution for modeling fracture. Navidtehrani et al. [27,28] recently proposed an ABAQUS User-defined Material (UMAT) implementation of the phase field fracture method. Although these models can successfully simulate the fracture behavior for linear-elastic solid materials, the adoption of similar framework on hyperelastic material would encounter convergence problems due to the nonlinear constitutive model of hyperelastic material, especially for hydrogel. Some researchers [29,30] have developed the non-commercial finite element code –so-called smoothed finite element method (S-FEM) for phase field fracture modeling for hyperelastic materials to circumvent convergence problem. However, the S-FEM method is not a standard finite element method and their codes are not open-sourced, which requires tedious work of programming. The phase field regularized cohesive zone model or rate-dependent modelling has also been developed for hyperelastic materials or hydrogel fracture [31–34]. Nonetheless, these non-commercial implementations require considerable amount of programming work for both the finite element solver and the Newton–Raphson solver, not exploiting most of commercial finite element software's in-built features.

In this work, we circumvent this issue by exploiting the analogy between the heat transfer law and the phase field evolution equation. This approach enables using the vast majority of ABAQUS' in-built features, including the coupled temperature-displacement elements from its finite element library, which avoids extra coding work on user-defined elements and the associated complications in meshing and visualization and also avoids coding Newton-Raphson solver, which can be troublesome for 3D cases. Moreover, the presented phase field implementation for hyperelastic materials can accommodate both staggered and monolithic solution schemes, ensuring convergence and accuracy in all cases. We demonstrate the potential and robustness of the presented solution by addressing several 2D and 3D boundary value problems for both hyperelastic materials and hydrogels. To verify our simulation, the experimental study on both hyperelastic material and hydrogel is designed and conducted and those data are compared with the corresponding simulation results.

The remainder of this manuscript is organized as follows. In Section 2 we describe the phase field model at large deformation and its numerical framework and finite element realization with the analogy of the heat transfer. Numerical fracture examples of hyperelastic materials are given in Section 3. Representative numerical fracture examples of hydrogels are shown in Section 4. In Section5, we conduct the experiment of the fracture of polydimethylsiloxane (PDMS) and hydrogel and compared them with the simulation. The manuscript ends with concluding remarks in Section 6.

2. Phase field fracture model for hyperelastic material and hydrogel

2.1. Phase field fracture model

The idea of approximating a sharp crack topology by a diffusive crack topology based on the introduction of a crack phase field d is motivated in Miehe et al. [15]. Following the idea that the crack propagation is not a discrete phenomenon, but initiates with micro-cracks and thus a continuous phenomenon, we introduce an exponential function to approximate the crack topology with consideration of an infinite one directional bar aligned along the $\times$ axis with a cross section:

$$d(x) = e^{-|x|/l_c}, \tag{1}$$

where l_c is the length scale parameter and $d(x)$ represents the so-called regularized or diffuse crack topology.

We then introduce a fracture surface density with the help of the phase field function by [35]:

$$\Gamma(d) = \int_{\Omega} \gamma(d, \nabla d) dV, \tag{2}$$

where $\gamma(d, \nabla d)$ is the crack surface density function.

A common choice for the crack surface density function $\gamma(d, \nabla d)$ is:

$$\gamma(d, \nabla d) = \frac{1}{2l_c} d^2 + \frac{l_c}{2} |\nabla d|^2 \tag{3}$$

It can be seen that the gradient of the phase field ∇d plays a significant role in the description, since this functional can easily be constructed by integrating a Galerkin-type weak form.

2.2. A framework of diffusive fracture for hyperelastic material and hydrogel

Based on the existing works on the phase field models for hyperelastic materials and hydrogel [29–34], we propose the following fracture framework. To couple the phase field fracture model with the large deformation problem, the potential free energy of a hyperelastic solid body can be written as:

$$\Pi^{int} = E(\mathbf{u}, d) + W(d), \tag{4}$$

where $E(\mathbf{u}, d)$ is the strain energy and $W(d)$ is the fracture energy.

Let $\Omega \subset R^{\delta}$ be the reference configuration of a material body with dimension $\delta \in [1, 2, 3]$, and $\partial\Omega \subset R^{\delta-1}$ its surface. The crack and the displacement fields are studied in the range of time $t \subset R$. Consequently, we introduce the time-dependent crack phase field:

$$d : \begin{cases} \Omega \times t \to [0, 1] \\ (\mathbf{x}, t) \to d(\mathbf{x}, t). \end{cases} \tag{5}$$

and the displacement field:

$$\mathbf{u} : \begin{cases} \Omega \times t \to R^{\delta} \\ (\mathbf{x}, t) \to \mathbf{u}(\mathbf{x}, t). \end{cases} \tag{6}$$

In Eq. (4), the internal potential energy can be written:

$$E(\mathbf{u}, d) = \int_{\Omega} \psi(\mathbf{F}, d) dV, \tag{7}$$

where $\mathbf{F}$ is the deformation gradient and $\psi(\mathbf{F}, d)$ is the potential energy density:

$$\psi(\mathbf{F}, d) = g(d) \cdot \psi_0(\mathbf{F}), \tag{8}$$

where $\psi_0(\mathbf{F})$ is an isotropic reference energy function associated with the undamaged elastic solid and $g(d)$ is a degradation function. The monotonically decreasing degradation function $g(d)$ describes the degradation of the stored energy with evolving damage. It is assumed to have the properties $g(0) = 1$; $g(1) = 0$; $g'(1) = 0$. A widely-used degradation function is $g(d)=(1\text{-}d)^2 + k$ [14,29,33], and k is a small number responsible for the stability of the solution.

In this work we do not consider anisotropic energy degradation (or sometimes referred to as asymmetric tension and compression energy release), because the examples are primarily tensile stress dominant and no compression induced crack of hyperelastic material is modelled. The same method has also been used for other hyperelastic material fracture research [30,33]. In this paper, the aim is to give a clear and transparent code which can then be developed either with anisotropic energy degradation [15], dynamic fracture [36] or fracture coupled with diffusion [33], therefore mostly isotropic energy degradation is considered.

For hyperelastic materials, such as the NeoHookean model, the energy function is taken:

$$\psi_0(\mathbf{F}) = \frac{1}{2} G(I_1 - 3) + \frac{1}{2} K(J - 1)^2, \tag{9}$$

where G is the shear modulus, K is the bulk modulus, $\mathbf{F}$ is the deformation gradient, $I_1 = \mathrm{tr}(\mathbf{F}^{\mathrm{T}}\mathbf{F})$ is the first invariant of right Cauchy–Green deformation tensor and $J = \det(\mathbf{F})$ is the determinant of the deformation gradient $\mathbf{F}$.

Due to damage, the free energy density is degraded during the fracture process. By calculating its first derivative, the Cauchy stress σ is given by:

$$\sigma = g(d) \cdot \sigma_0 = g(d) \cdot J^{-1} \left(\frac{\partial \psi_0(\mathbf{F})}{\partial \mathbf{F}} \mathbf{F}^{\mathrm{T}} \right) = \left[(1 - d)^2 + k \right] \cdot J^{-1} \left[G \cdot \mathbf{F}^T \mathbf{F} + K(J - 1)\mathbf{1} \right]. \tag{10}$$

For hydrogel, we consider the following free energy density function:

$$\psi_0(\mathbf{F}) = \frac{1}{2} N k_B T \left[\mathbf{F}^T \mathbf{F} - 3 - 2\ln(\det \boldsymbol{F}) \right] + k_B T \left(C \ln\left(\frac{\nu C}{1 + \nu C} \right) + \frac{\chi C}{1 + \nu C} \right) - \mu C, \tag{11}$$

where N is the referential chain density and $k_B T$ is the temperature in the unit of energy; k_B the Boltzman constant; and T the absolute temperature; ν is the nominal volume of a solvent molecule, C is the concentration of the solvent in the gel, χ is the interaction parameter, and μ is the chemical potential in the solvent.

We recall that Nk_BT denotes the shear modulus of the network in hydrogel. The volumetric change due to physical association of the molecules is small compared to the volumetric change due to imbibing molecules. These considerations together suggest an idealization: All molecules in a gel are incompressible, and the volume of the gel is the sum of the volume of the dry network and the volume of the pure liquid solvent. This idealization is written as:

$$1 + \nu C = \det(\boldsymbol{F}). \tag{12}$$

The molecular incompressibility of the hydrogel is not to be confused with the incompressibility of an elastomer. Unlike an elastomer, a gel can undergo an enormous change in volume by imbibing a solvent. The molecular incompressibility of a hydrogel simply means that the volume of the gel equals the sum of the volumes of individual molecules of the network and the solvent.

The free energy density of hydrogel is also degraded during the fracture process. By calculating its first derivative, the Cauchy stress of hydrogel is given by:

$$\sigma = \left[(1 - d)^2 + k \right] \cdot \left[\frac{N k_B T}{J} (\mathbf{F}^T \mathbf{F} - \mathbf{1}) + \frac{k_B T}{\nu} \left[\ln\left(\frac{J - 1}{J} \right) + \frac{1}{J} + \frac{\chi}{J^2} - \frac{\mu}{k_B T} \right] \mathbf{1} \right]. \tag{13}$$

The second term in Eq. (4) stands for the energy due to fracture and can be calculated as:

$$W(d) = \int_{\Omega} g_c \gamma(d, \nabla d) dV, \tag{14}$$

where W is the sum of all the fracture surfaces multiplied by g_c, the critical energy release rate.

We introduce the external component of the potential energy as follows:

$$\Pi^{\text{ext}} = P(\mathbf{u}) = \int_{\Omega} \bar{\gamma} \cdot \mathbf{u} dV + \int_{\partial\Omega} \bar{\mathbf{t}} \cdot \mathbf{u} dA \tag{15}$$

where $\bar{\gamma}$ and $\bar{\mathbf{t}}$ are the prescribed volume force and boundary force respectively.

2.3. The monolithic and staggered schemes for phase field facture

To have a stable implicit formulation, the finite element solution is decoupled as three parts: the displacement field, the history field and the phase field. The schematic illustration for phase field fracture problem in hyperelastic solids is shown in Fig. 1. Γ is the face of the crack. $\Gamma_{\mathbf{u}}$ and $\Gamma_{\mathbf{t}}$ are the surface boundaries of the displacement field. The problem can be split into two quasi-independent minimization procedures. First, we need to solve the fracture topology:

$$\Pi^{int} \cong \Pi^{d} = \int_{\Omega} \left[g_c \gamma(d, \nabla d) + (1-d)^2 H \right] dV \tag{16}$$

where we use a so-called history variable:

$$H = \begin{cases} \psi_0(\mathbf{F}) \text{ if } \quad \psi_0(\mathbf{F}) > H_n \\ \quad H_n \text{ otherwise}, \end{cases} \tag{17}$$

where H_n is the previously calculated energy history at step n. This field weakly couples the displacement and phase field and it enables the damage irreversibility.

In a quasi-state, with a fixed d, the displacement field is calculated:

$$E(\mathbf{u}, d) - \Pi^{\text{ext}} \cong \Pi^{u} = \int_{\Omega} [\psi(\mathbf{F}, d) - \bar{\gamma} \cdot \mathbf{u}] dV - \int_{\partial\Omega} \bar{\mathbf{t}} \cdot \mathbf{u} dA \tag{18}$$

By taking the variation of the energy of both fields ($\delta\Pi^{u} = 0, \delta\Pi^{d} = 0$), the corresponding displacement field governing equation is written as:

$$\nabla\sigma - \bar{\gamma} = 0 \tag{19}$$

with boundary conditions $\mathbf{u} = \bar{\mathbf{u}}$ on $\Gamma_{\mathbf{u}}$ and $\sigma \cdot \mathbf{n} = \bar{\mathbf{t}}$ on $\Gamma_{\mathbf{t}}$ with $\mathbf{n}$ the outward normal of the external surface.

The corresponding phase field governing equation is written as:

$$\frac{g_c}{l_c}\left(d - l_c^2 \Delta d\right) = 2(1-d)H \tag{20}$$

with the boundary condition $\nabla d \cdot \mathbf{n} = 0$ onΓ.

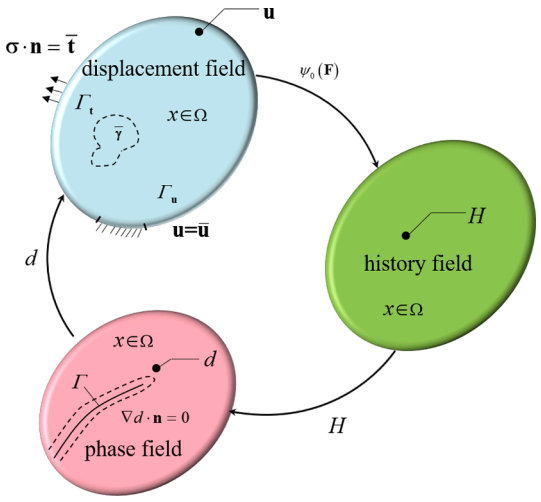

Fig. 1. Illustration of the split scheme for phase field problem in hyperelastic solids.

The phase field model at large deformation framework can be solved in either a monolithic or a staggered manner. In a monolithic scheme, the displacement field and the phase field are solved simultaneously (Fig. 2). On the other hand, a staggered scheme entails an alternative minimisation approach, by which the displacement and phase fields are solved sequentially (Fig. 2). Monolithic solution strategies are unconditionally stable and, therefore, more efficient (in principle). However, the total potential energy functional (3) is non-convex with respect to **u** and d, making the Jacobian matrix in Newton's method becomes indefinite, which can cause a convergence problem when solving for the displacement and the phase field at the same time. In order to relieve the convergence problem, we also study the staggered scheme. In the staggered case, the residual and the stiffness matrix for the phase field sub-system are built considering the history field of the previous increment H_n, meaning the history field is frozen during the iterative procedure, which is in favour of convergence at the cost of scarifying unconditional stability. A recursive iteration or multi-pass staggered scheme can be implemented by transferring the history field between the hyperelastic user subroutine (UHYPER) and the heat flux subroutine (HETVAL) in ABAQUS. The differences in performance between these two solution schemes, are addressed in the numerical examples in Section 3.

2.4. Finite element discretization in UHYPER and heat transfer analogy

In Section 2.4, we will describe the finite element discretization in ABAQUS and its corresponding heat transfer analogy. First, we introduce the implementation of the framework in UHYPER subroutine, where a history field is specified to ensure damage irreversibility.. Secondly, the analogy with heat transfer is presented.

Based on the variables at time t_n, a new phase field is calculated at t_{n+1}:

$$d_{n+1} = Arg\left\{ \inf_{d} \int_{\Omega} \left[g_c \gamma(d, \nabla d) + (1-d)^2 H \right] dV \right\}, \tag{21}$$

where the history field (H)is calculated according to Eq. (14). Then the new phase field can be solved as:

$$\mathbf{K}_n^d \mathbf{d}_{n+1} = -\mathbf{r}_n^d, \tag{22}$$

where $\mathbf{d}_{n+1}$ is the new phase field value of the solution in the Newton method; $\mathbf{r}_n^d$ is the residue and $\mathbf{K}_n^d$ is the tangent stiffness at time t_n.

Based on the variables at time t_n, a new phase field is calculated at t_{n+1}:

$$u_{n+1} = Arg\left\{ \inf_{u} \int_{\Omega} [\psi(\mathbf{F}, d) - \bar{\gamma} \cdot \mathbf{u}] dV - \int_{\partial\Omega} \bar{\mathbf{t}} \cdot \mathbf{u} dA \right\}. \tag{23}$$

Similar to the phase field, this problem can be solved by a simple linearization:

$$\mathbf{K}_n^u \mathbf{u}_{n+1} = -\mathbf{r}_n^u, \tag{24}$$

In the Newton-Raphson algorithm, we need to update the tangent matrix and the residue vector at each internal iteration:

$$\begin{bmatrix} \mathbf{K}_n^d & \mathbf{0} \\ \mathbf{0} & \mathbf{K}_n^u \end{bmatrix} \begin{bmatrix} \mathbf{d}_{n+1} \\ \mathbf{u}_{n+1} \end{bmatrix} = - \begin{bmatrix} \mathbf{r}_n^d \\ \mathbf{r}_n^u \end{bmatrix} \tag{25}$$

The corresponding residue vector for the phase field is formulated as:

$$\mathbf{r}^d = \int_{\Omega} \left\{ \left[\frac{g_c}{l_c} d - 2(1-d)H \right] \left(\mathbf{N}^d\right)^T + g_c l_c \left(\mathbf{B}^d\right)^T \nabla d \right\} dV \tag{26}$$

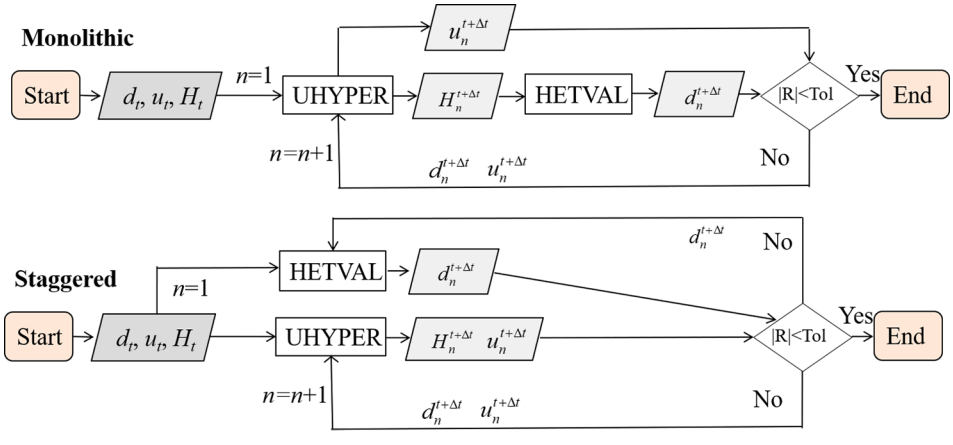

Fig. 2. Flowchart of the monolithic and staggered scheme used to implement the coupled displacement-phase field solution in Abaqus.

where $\mathbf{N}^d$ is the vector of the shape functions:$\mathbf{N}^d = [N_1 ... N_b]$ (where b = 4 for 2D and b = 8 for 3D) and $\mathbf{B}^d$ is a matrix with the spatial derivatives.

The phase field values of the solution in the Newton method are defined as:$d = \mathbf{N}^d\mathbf{d}$, where $\mathbf{d}$ contains phase field values on each element node. The local gradient reads similarly as:$\nabla d = \mathbf{B}^d\mathbf{d}$.

The tangent matrix of the phase field is then calculated as:

$$\mathbf{K}^d = \int_\Omega \left\{ \left[\frac{g_c}{l_c} + 2H \right] (\mathbf{N}^d)^T \mathbf{N}^d + g_c l_c (\mathbf{B}^d)^T \mathbf{B}^d \right\} dV \tag{27}$$

The corresponding residue vector for the displacement field is formulated as:

$$\mathbf{r}^u = \int_\Omega \left\{ \left[(1-d)^2 + k \right] (\mathbf{B}^u)^T \sigma_0 - (\mathbf{N}^u)^T \cdot \bar{\gamma} \right\} dV - \int_{\partial\Omega} (\mathbf{N}^u)^T \cdot \bar{\mathbf{t}} dA \tag{28}$$

Finally we give the tangent matrix for the displacement field solution:

$$\mathbf{K}^u = \int_\Omega \left\{ \left[(1-d)^2 + k \right] (\mathbf{B}^u)^T \frac{\partial \sigma_0}{\partial \mathbf{u}} \mathbf{B}^u \right\} dV - \int_{\partial\Omega} (\mathbf{N}^u)^T \cdot \mathbf{N}^u \cdot \frac{\partial \bar{\mathbf{t}}}{\partial \mathbf{u}} dA \tag{29}$$

Although the proposed UHYPER/HETVAL framework does not write the tangent matrix and the residue matrix on the integration point level, we also study the UEL and UMAT methods (codes provided in the Supplementary material), which do need those matrixes. Moreover, we want to provide a deep and thorough understanding of the framework, which helps the proposed framework to be extended to relevant studies in the future. For example, a UHYPER + HETVAL/UEL framework can be studied with the added UEL subroutine to solve the diffusion field for the hydrogel fracture coupled with diffusion study in the future.

In the UHYPER implementation for hyperelastic material model, we need to provide the free energy density and its derivatives with respect to the first, second, and the third strain invariants (invariants of right Cauchy–Green deformation tensor). For a classical NeoHookean material, the free energy density could be thus rewritten as:

$$\psi_0(F) = \frac{1}{2} G \left(J^{\frac{2}{3}} \bar{I}_1 - 3 \right) + \frac{1}{2} K (J-1)^2, \tag{30}$$

where $\bar{I}_1 = I_1 J^{-2/3}$ is the first strain invariant defined in ABAQUS.

First derivatives are listed as follow,

$$\frac{\partial \psi_0}{\partial \bar{I}_1} = \frac{1}{2} G J^{\frac{2}{3}}, \frac{\partial \psi_0}{\partial \bar{I}_2} = 0, \frac{\partial \psi_0}{\partial J} = \frac{1}{3} G \bar{I}_1 J^{-\frac{1}{3}} + K(J-1). \tag{31}$$

Second derivatives are listed as follow,

$$\frac{\partial^2 \psi_0}{\partial \bar{I}_1^2} = 0, \frac{\partial^2 \psi_0}{\partial \bar{I}_2^2} = 0, \frac{\partial^2 \psi_0}{\partial J^2} = -\frac{1}{9} G \bar{I}_1 J^{-\frac{4}{3}} + K, \frac{\partial^2 \psi_0}{\partial \bar{I}_1 \partial \bar{I}_2} = 0, \frac{\partial^2 \psi_0}{\partial \bar{I}_1 \partial J} = \frac{1}{3} G J^{-\frac{1}{3}}, \frac{\partial^2 \psi_0}{\partial \bar{I}_2 \partial J} = 0 \tag{32}$$

Third derivatives are listed as follow,

$$\frac{\partial^3 \psi_0}{\partial \bar{I}_1^2 \partial J} = 0, \frac{\partial^3 \psi_0}{\partial \bar{I}_1 \partial \bar{I}_2 \partial J} = 0, \frac{\partial^3 \psi_0}{\partial \bar{I}_1 \partial J^2} = -\frac{1}{9} G J^{-\frac{4}{3}}, \frac{\partial^3 \psi_0}{\partial \bar{I}_2^2 \partial J} = 0, \frac{\partial^3 \psi_0}{\partial J^3} = -\frac{4}{27} G \bar{I}_1 J^{-\frac{7}{3}}. \tag{33}$$

For the hydrogel constitutive model, to avoid singularity in the dry state, we assume an initial free swelling condition of hydrogel, the deformation gradient at this state is defined as:

$$\boldsymbol{F}_0 = \begin{bmatrix} \lambda_0 & 0 & 0 \\ 0 & \lambda_0 & 0 \\ 0 & 0 & \lambda_0 \end{bmatrix} \tag{34}$$

where λ_0 is the initial isotropic stretch of the gel.

Relative to the initial free swelling state, the current deformation of the gel is, as measured by ABAQUS,$\boldsymbol{F}'$. To obtain the actual deformation gradient of the gel, we write$\boldsymbol{F} = \boldsymbol{F}'\boldsymbol{F}_0$. Therefore, in all subsequent implementations in ABAQUS, we write$J = \lambda_0^3 J'$, where J denotes the actual swelling ratio and J' denotes the swelling ratio used in ABAQUS. This approach has been used by many hydrogel simulation studies [37–39]. The nondimensionalized free energy density is thus rewritten as:

$$\frac{\psi_0 \nu}{k_B T} = \frac{1}{2} N \nu \left[\lambda_0^2 J'^{\frac{2}{3}} \bar{I}_1 - 3 - 2\ln\left(\lambda_0^3 J'\right) \right] + \left(\lambda_0^3 J' - 1\right) \left(\ln \frac{\lambda_0^3 J' - 1}{\lambda_0^3 J'} + \frac{\chi}{\lambda_0^3 J'} - \frac{\mu}{k_B T} \right), \tag{35}$$

where $\mu / k_B T$ can be taken as the dimensionless form for chemical potential.

First derivatives are the following,

$$\frac{\partial(\psi_0\nu/k_BT)}{\partial\bar{I}_1}=\frac{1}{2}N\nu\lambda_0^2J^{'\frac{2}{3}},\frac{\partial(\psi_0\nu/k_BT)}{\partial\bar{I}_2}=0, \tag{36}$$

$$\begin{aligned}\frac{\partial(\psi_0\nu/k_BT)}{\partial J^{'}}=&\frac{1}{2}N\nu\left(\frac{2}{3}\lambda_0^2J^{'-\frac{1}{3}}\bar{I}_1-\frac{2}{J^{'}}\right)+\left(\lambda_0^3J^{'}-1\right)\left[\frac{\lambda_0^3}{\lambda_0^3J^{'}-1}-\frac{1}{J^{'}}-\frac{\chi}{\lambda_0^3J^{'2}}\right]\\&+\lambda_0^3\left[\ln\frac{\lambda_0^3J^{'}-1}{\lambda_0^3J^{'}}+\frac{\chi}{\lambda_0^3J^{'}}-\frac{\mu}{k_BT}\right].\end{aligned} \tag{37}$$

Second derivatives are the following,

$$\frac{\partial^2(\psi_0\nu/k_BT)}{\partial\bar{I}_1^2}=0,\frac{\partial^2(\psi_0\nu/k_BT)}{\partial\bar{I}_2^2}=0, \tag{38}$$

$$\begin{aligned}\frac{\partial^2(\psi_0\nu/k_BT)}{\partial J^{'2}}=&\frac{1}{2}N\nu\left(-\frac{2}{9}J^{'-\frac{4}{3}}\bar{I}_1+\frac{2}{J^{'2}}\right)+\left(\lambda_0^3J^{'}-1\right)\left[-\frac{\lambda_0^6}{\left(\lambda_0^3J^{'}-1\right)^2}+\frac{1}{J^{'2}}+\frac{2\chi}{\lambda_0^3J^{'3}}\right]\\&+2\lambda_0^3\left[\frac{\lambda_0^3}{\lambda_0^3J^{'}-1}-\frac{1}{J^{'}}-\frac{\chi}{\lambda_0^3J^{'2}}\right],\end{aligned} \tag{39}$$

$$\frac{\partial^2(\psi_0\nu/k_BT)}{\partial\bar{I}_1\partial\bar{I}_2}=0,\frac{\partial^2(\psi_0\nu/k_BT)}{\partial\bar{I}_1\partial J^{'}}=\frac{1}{3}N\nu\lambda_0^2J^{'-\frac{1}{3}},\frac{\partial^2(\psi_0\nu/k_BT)}{\partial\bar{I}_2\partial J^{'}}=0. \tag{40}$$

Third derivatives are the following,

$$\frac{\partial^3(\psi_0\nu/k_BT)}{\partial\bar{I}_1^2\partial J^{'}}=0,\frac{\partial^3(\psi_0\nu/k_BT)}{\partial\bar{I}_2^2\partial J^{'}}=0,\frac{\partial^3(\psi_0\nu/k_BT)}{\partial\bar{I}_1\partial\bar{I}_2\partial J^{'}}=0, \tag{41}$$

$$\frac{\partial^3(\psi_0\nu/k_BT)}{\partial\bar{I}_1\partial J^{'2}}=N\nu\left(-\frac{1}{9}\lambda_0^2J^{'-\frac{4}{3}}\right),\frac{\partial^3(\psi_0\nu/k_BT)}{\partial\bar{I}_2^2\partial J^{'}}=0, \tag{42}$$

$$\begin{aligned}\frac{\partial^3(\psi_0\nu/k_BT)}{\partial J^{'3}}=&\frac{1}{2}N\nu\left(\frac{8}{27}J^{'-\frac{4}{3}}\bar{I}_1-\frac{4}{J^{'3}}\right)+\left(\lambda_0^3J^{'}-1\right)\left[\frac{2\lambda_0^9}{\left(\lambda_0^3J^{'}-1\right)^2}-\frac{2}{J^{'3}}-\frac{6\chi}{\lambda_0^3J^{'4}}\right]\\&+3\lambda_0^3\left[-\frac{\lambda_0^6}{\left(\lambda_0^3J^{'}-1\right)^2}+\frac{1}{J^{'2}}+\frac{2\chi}{\lambda_0^3J^{'3}}\right].\end{aligned} \tag{43}$$

With Eqs. (30) – (43) for the undamaged elastic solid free energy density ψ_0 and its derivatives, a user subroutine is coded in the format of UHYPER in ABAQUS for NeoHookean and hydrogel materials respectively. According to Eq. (8), the function *g(d)* is taken into account for the potential energy density $\psi(\mathbf{F},d)$ and its derivatives on the element level, which will be used by ABAQUS to calculate the stress on the integration level.

For a solid with the thermal conductivityκ, specific heat c_p and densityρ, the field equation for heat transfer in the presence of a heat source r is specified as:

$$\kappa\nabla^2T-\rho c_p\frac{\partial T}{\partial t}=r \tag{44}$$

where T is the temperature field. Under steady-state condition, the rate term vanishes and Eq. (44) is reduced to,

$$\kappa\nabla^2T=r \tag{45}$$

We can easily notice the analogy between this elliptic partial differential equation (PDE) with the phase field evolution law, with the temperature field acting as the phase field $T=d$. Making use of the history field described above, one can reformulate the phase field governing equation in current configuration, Eq. (20), as.

$$\nabla^2 d = \frac{d}{l_c^2} - \frac{2(1-d)H}{g_c l_c}. \tag{46}$$

For Eq. (45), heat flux, r, is not a source-free one but a temperature (T) related one, just like the phase field evolution Eq. (46) is a function of unknown d. And thus Eqs. (44) and (45) are equivalent upon assigning the value of unity to the thermal conductivity ($\kappa = 1$) and defining the following heat flux due to internal heat generation,

$$r = \frac{d}{l_c^2} - \frac{2(1-d)H}{g_c l_c}. \tag{47}$$

Finally, for the computation of the residue vectors and stiffness matrices, we should also define the rate of change of heat flux (r) with temperature ($T = d$),

$$\frac{\partial r}{\partial d} = \frac{1}{l_c^2} + \frac{2H}{g_c l_c}. \tag{48}$$

We have restricted the study to the steady-state scenario, treating the phase field evolution law as rate-independent. This is, by far, the most common formulation for hyperelastic phase field fracture.

The heat transfer analogy described can be readily implemented in ABAQUS by making use of hyperelastic user subroutine (UHYPER) and heat flux subroutine (HETVAL). The process is outlined in Fig. 3. Taking advantage of the heat transfer analogy enables carrying out the implementation at the element level, using in-built displacement-temperature elements such as the ABAQUS CPS4T type for the 2D case of 4-node bilinear quadrilateral elements. For a given element, ABAQUS provides to the integration point-level subroutines the values of strain invariant and phase field (temperature), as interpolated from the nodal solutions. Within each integration point loop, the hyperelastic user subroutine (UHYPER) is called first. Inside the UHYPER, the strain energy density function $\psi_0(\mathbf{F})$ and its derivatives with respect to first, second and third strain invariants can be readily computed. The current value of the phase field (temperature) is then used to account for the damage degradation of these quantities. The strain energy density, the current value of the phase field and other necessary parameters (l_c, g_c) can be stored in so-called solution dependent state variables (SDVs), enabling to enforce the irreversibility condition. In the HETVAL subroutine we define the internal heat flux r, Eq. (47), and its derivative with respect to the temperature (phase field)$\partial r/\partial d$, Eq. (48). The process is repeated for every integration point, enabling ABAQUS to externally build the element stiffness matrices $\mathbf{K}$ and residuals $\mathbf{R}$ and assemble the global system of equations (Fig. 3).

It is worth emphasising that the phase field and the displacement field is only weakly coupled in our framework ($\mathbf{K}_n^{ud} = \mathbf{K}_n^{du} = 0$), making the stiffness matrix symmetric. By default, a non-symmetric system for coupled displacement-temperature analyses is assumed in ABAQUS but this can be modified by defining a separated solution technique (Details can be found in Step module of the input file in the Supplementary data).

It should be noted that no additional pre-processing or post-processing steps are needed, all actions can be done within the ABAQUS/CAE graphical user interface and the phase field solution can be visualised by plotting the nodal solution temperature (NT11) in the visualization module.

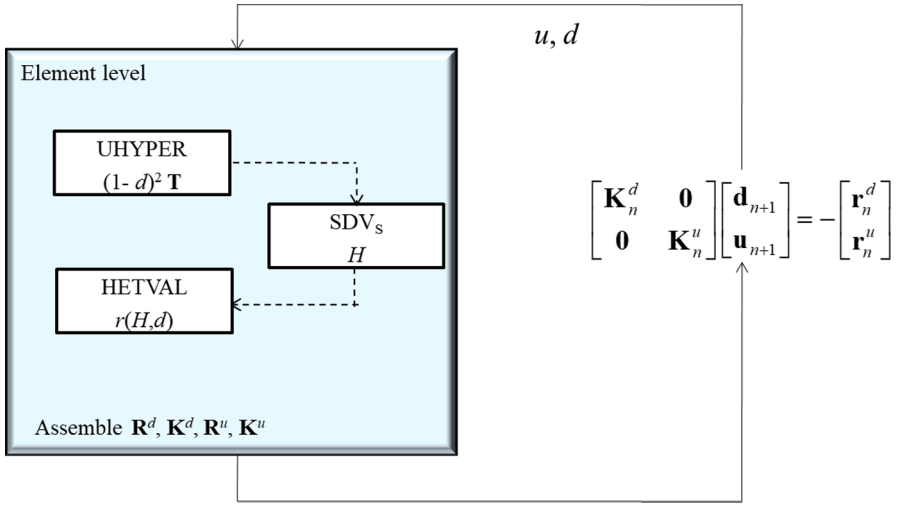

Fig. 3. User subroutine flowchart for the implementation of a coupled deformation-phase fields model exploiting the analogy with heat transfer module.

3. Numerical fracture examples of hyperelastic materials

3.1. One element test

One 2D plane stress element is the simplest case, in which the phase field based large deformation model is investigated in-depth concerning the nominal stress and damage evolution. In Fig. 4a, the boundary conditions and the geometry are shown. The dimensions of the element are 10×10 mm in both $\times$ and y direction. The bottom nodes are constrained in both directions, whereas we allow the top nodes to deform vertically.

The shear modulus of the specimen is set to $G = 0.4$ MPa and the bulk modulus is set to $K = 4$ Mpa. The critical energy release rate is $g_c = 2.4$ N/mm and the length scale parameter is $l_c = 1$ mm. The above material parameters are reasonable values verified by many hyperelastic material fracture studies [29,40].

It should be noted that in this example it is not our aim to show actual fracture patterns, we only demonstrate the elementary evolutions of the stress and damage in the phase field model. For consistency purpose, all the examples shown in Section 3 use the following set of parameters ($G = 0.4$ MPa, $K = 4$ Mpa, $g_c = 2.4$ N/mm and $l_c = 1$ mm). The deformation is applied in $1000 \times \Delta u_y$ steps, where $\Delta u_y = 1.9 \times 10^{-1}$ mm. The input and the source files are available for this example in the Supplementary directory. The practical details are discussed in Appendix A.

We use one 4-node 2D plane stress CPS4T element to represent the block of the hyperelastic material. Fig. 4a shows the nominal stress computed by staggered and monolithic schemes. A very good agreement can be found between those two methods. The difference of the number of iterations to achieve convergence between those two methods will be shown and discussed in Section 3.2.

Also, the irreversibility damage condition is shown in Fig. 4a and Fig. 4b. When the applied force is unloaded and then reloaded, the amplitude shows that after certain damage, the unload path is different from the initial undamaged loading path, and the reload path is the same as the unload path, indicating the irreversibility damage condition. When the reloading stretch exceeds the historical maximum loading stretch, the hyperelastic material starts get further damaged and the loading curve follows again the initial loading curve. Finally, Fig. 4b shows the governing phase field damage as a function of the applied axial stretch. It can be observed that as stretch λ_y approaches 20, the damage value gradually approaches 1, which means the material has achieved fully degraded.

3.2. Single edge notched test

In this case, we test the effectiveness of our phase-field model by performing the fracture analyses of the single edge cracked tensile sample. The geometry of the sample is depicted in Fig. 5a. The initial crack length is 20 mm and the bottom side of the rectangular specimen is fixed, while the top side is moved with the length of the top side fixed. This experimental setup is also known as pure shear. The location of the cracks (red line), the symmetry boundary conditions, and the displacement boundary conditions are in indicated in Fig. 5a. In our simulation we exploited the symmetry of the specimen and discretized half of the specimen with approximately 4700 elements. The shape of the element is quadrilateral element dominated, with approximately 90 triangular elements (The input file is included in the Supplementary material). The parameters are taken the same as that of Section 3.1. The region around the crack path is refined in order to reach the maximum of $h = 0.1$ mm mesh size. It should be noted that the simulation of the hyperelastic material's fracture is very sensitive to the length of the steps and very small step lengths is preferred for the aim of convergence.

The deformed configurations of the specimen at different time steps are depicted in Fig. 5, which shows the crack evolution until the final rupture. Fig. 5b shows vividly the large deformation of a hyperelastic material. Up to this deformation, the fracture phase field is virtually undeveloped. The applied deformation is $u = 4.791$ mm in Fig. 5b. Fig. 5c shows the deformed configuration of the system

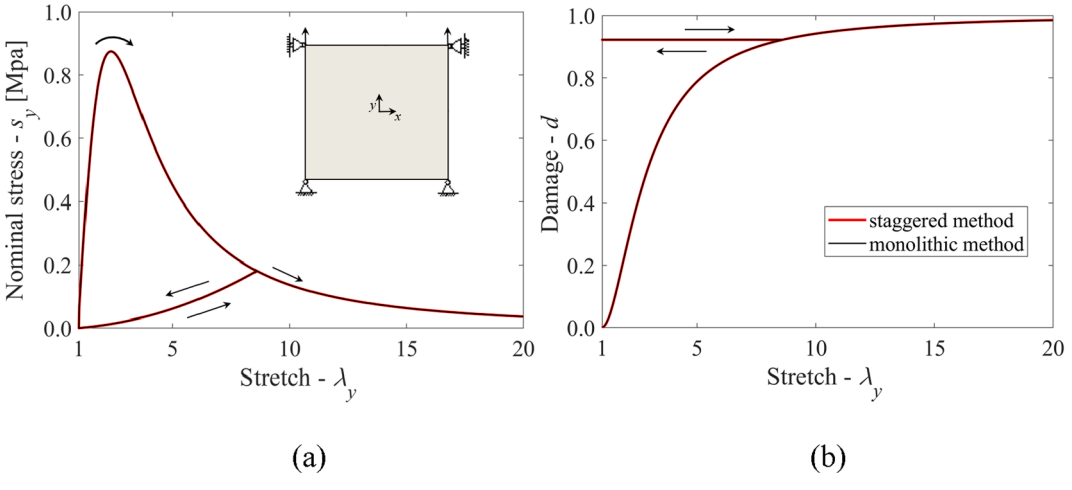

Fig. 4. (a) The nominal stress as a function of axial stretch in y direction for one element subjected to uniaxial tension. (b) Damage phase field as a function of applied axial stretch λ_y.

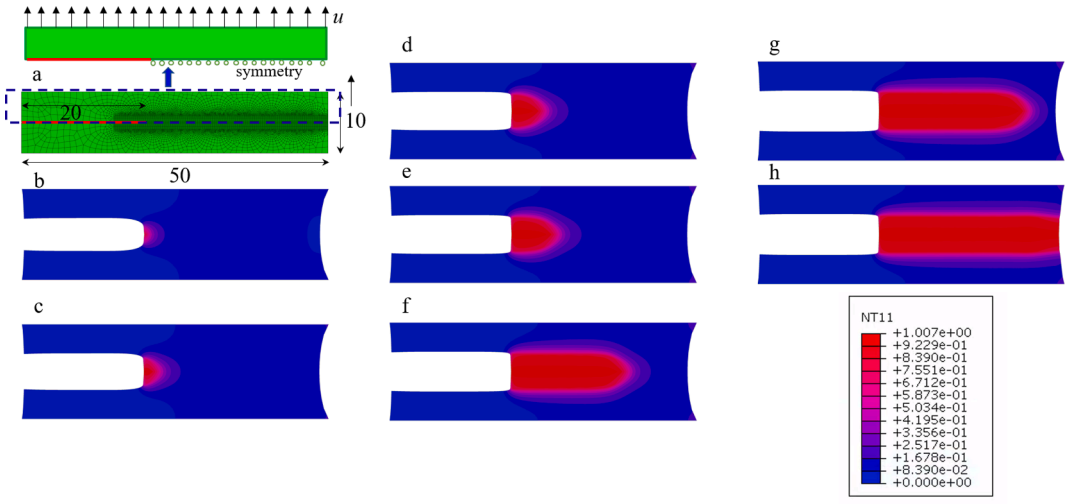

Fig. 5. (a) The geometry (mm) of the single edge notched tension test. Crack pattern at displacement of (b) $u = 4.791$ mm; (c) $u = 5.400$ mm; (d) $u = 5.680$ mm, (e) $u = 5.760$ mm, (f) $u = 6.020$ mm, (g) $u = 6.116$ mm, and finally (h) $u = 6.1184$ mm for a length scale of $l_c = 1$ mm and an effective element size $h = 0.1$ mm.

and the contour of the phase field after an overall deformation of $u = 5.400$ mm. The phase field begins to develop in the area near the initial notch. For an applied deformation of $u = 5.680$ mm the fracture phase field is fully developed in the vicinity of the horizontal notch, Fig. 5d.

Once the fracture phase field has reached a value representing fully damaged material, a drastic increase in crack growth occurs. Fig. 5e–h reports the system at prescribed boundary displacements of $u = 5.760$ mm, 6.020 mm, 6.116 mm, and finally 6.1184 mm. The crack is propagating continuously until the body has separated into two parts. To make the visualization of crack opening more clearly shown, the contour plot label of the fracture phase field d (NT11) is shown in Fig. 5 for reference.

We also compared the computation efficiency of the proposed staggered and monolithic schemes. The size of each increment and the number of iterations that were needed to achieve convergence is shown in Fig. 6. While the entire crack propagation process can be captured, for both methods, many increments require a very significant number of iterations to achieve convergence. Nonetheless, the staggered implementation appears to be more robust and efficient than the monolithic method, in which the calculation appears divergent after 5000 interactions during the crack propagation state and smaller iteration step is required during unstable cracking. It should be noted that the simulation results are incremental step time-dependent. For the convergence criterion: maximum number of iterations allowed in two consecutive increments is 5000 with a small enough load step ($\Delta u = 0.0002$ mm). For consistency purpose, all the examples shown later choose the staggered method and the convergence-related parameters of all cases in this article are set the same.

Fig. 6 also shows the number of iterations required to achieve convergence in each increment. We use time increments of constant

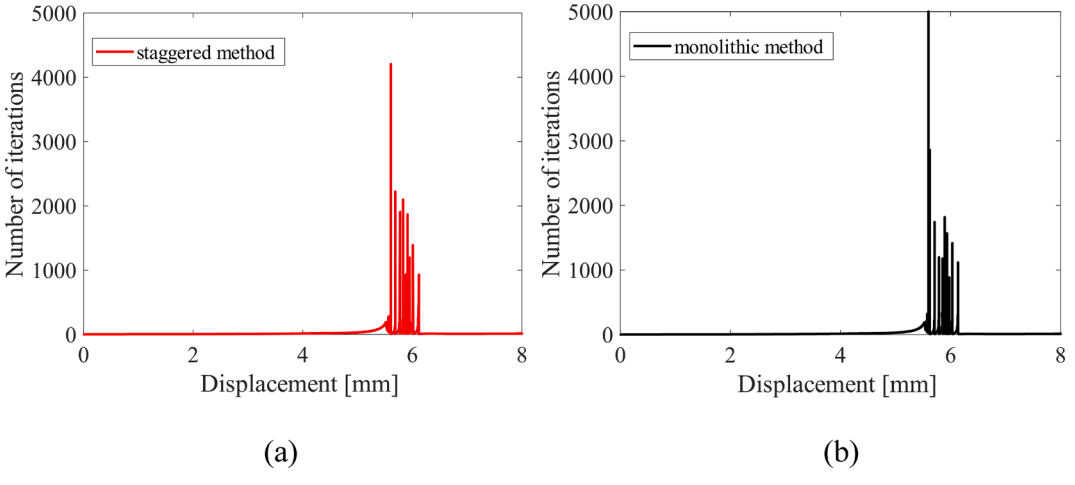

Fig. 6. The single edge notched tension test: (a) Number of iterations per increment for the staggered scheme; (b) number of iterations per increment for the monolithic scheme with the maxium iteration 5,000.

size and resolve the analysis with a total of 10,000 load increments. Convergence throughout can be achieved with as few as 2 increments, but using a larger number facilitates capturing the sudden load drop with greater fidelity. An adaptive time stepping scheme is also incorporated. This will allow for the increment size to increase or decrease as needed, enabling accurate results at an even smaller computational cost. In any case, it can be observed that the problem can be solved efficiently, with most time increments requiring a small number of iterations to achieve convergence (10 or fewer). However, resolving the fracture event requires a load increment with over 4000 iterations.

3.3. Double notched tensile test

In this section, we demonstrate the damage evolution of the double notched tensile test. The geometric setup is depicted in Fig. 7a where all dimensions are given in the unit of [mm]. The initial crack length is set as 16 mm. In our simulation, we exploited the symmetry of the specimen and discretized one-quarter of the specimen with 9565 elements. Similar to Section 3.2, the location of the cracks (red line), the symmetry boundary conditions, and the displacement boundary conditions are in indicated in Fig. 7a. The shape of the element is quadrilateral element CPS4T dominated, with approximately 90 triangular elements CPS3T (the input file is included in the Supplementary material). In order to capture the crack pattern properly, the mesh is refined where the crack is expected to propagate. In the critical zone, an effective element size of $h = 0.1$ mm is chosen. The length-scale parameter lc applied in the simulations is 1 mm resembling 10 elements. The parameters are set as the same as that of Section 3.1. Compared with the examples in Section 3.2, the double notched tensile simulation encounters more convergence difficulty due to the strong boundary constraints. To levigate the convergence problem, the automatic stabilization module with the damping factor in ABAQUS is exploited while the adaptive meshing method and restart schemes cannot lead to efficiency improvements.

Fig. 7 shows the resulting crack pattern with the initial crack of 16 mm. The visualization contour label of the fracture phase field d (NT11) is set the same as that of Section 3.2 for reference. Fig. 7 b–c show the elastic deformation of the specimen until an overall deformation of $u = 52.326$ mm at which the crack initiates. The contour plot shows that the damage field is developed to some amount around the initial notch tip with no crack propagation at this stage. Fig. 7d represents the beginning of the fracture as the damage field exceeds the level set the first time at an overall deformation of $u = 58.080$ mm. After this point the crack is drastically propagating. Fig. 7e–j depict the subsequent propagation of the crack until the hyperelastic material has been separated into two parts.

3.4. 3D single notched plate

Similar to the 2D case, a 3D single edge notched specimen is studied with a mode I crack. The location of the cracks is the same with 5 mm width. In our simulation, we exploited the symmetry of the specimen and discretized only one-quarter of the specimen, shown in Fig. 8a. The displacement boundary conditions is apply on the entire face shown in Fig. 8a. The material properties are the same as that of Section 3.1 with the mesh of 6250 C3D8HT elements, and the refinement of $h = 0.1$ mm. It should be noted that under the coupled

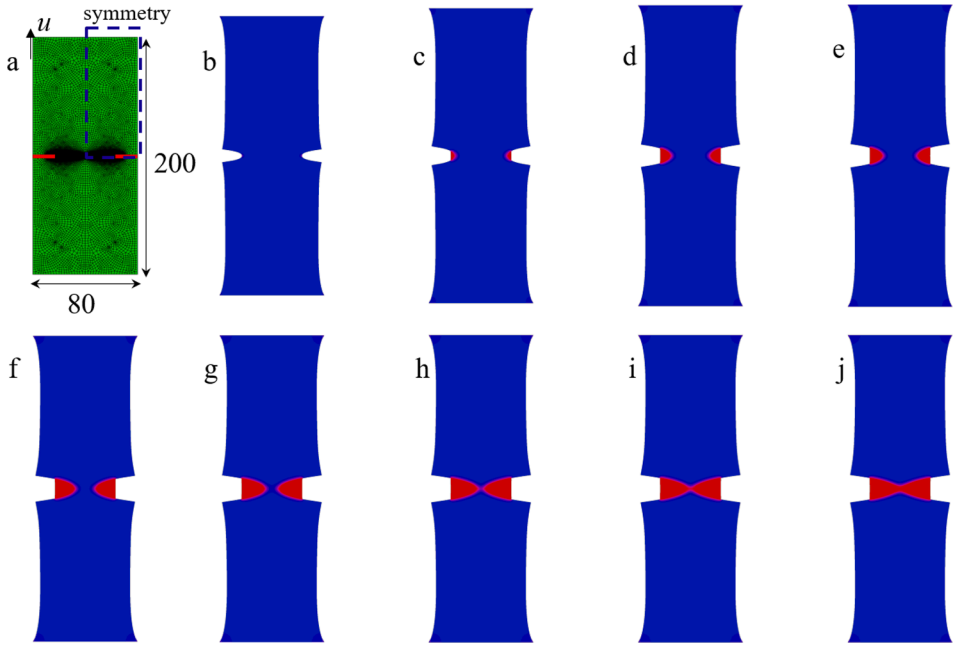

Fig. 7. (a) The geometry of the double edges notched tension test. The crack pattern of double edge notch tension specimen with the initial notch width of 16 mm. The snapshots (b)–(j) are at applied deformation of $u = 35.4060$ mm, $u = 52.326$ mm, $u = 53.640$ mm, $u = 54.702$ mm, $u = 57.246$ mm, $u = 58.080$ mm, $u = 58.494$ mm, $u = 58.566$ mm, $u = 58.638$ mm. Effective element size of 0.1 mm and length scale of 1 mm.

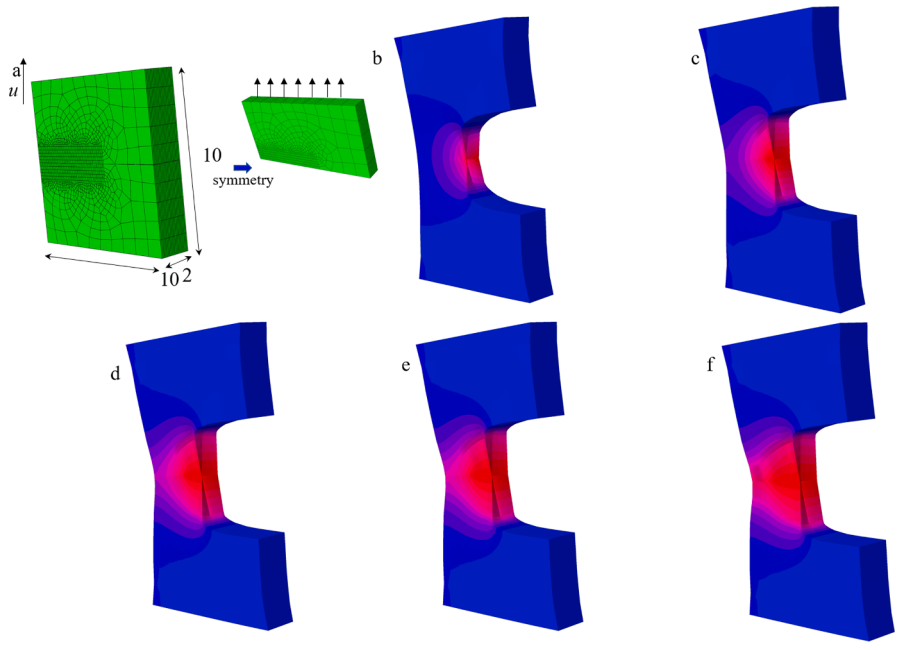

Fig. 8. (a) The geometry (mm) of the 3D single edge notched tension test with the initial notch of 5 mm width. The crack pattern of double edge notch tension specimen with the initial notch of 5 mm width. The snapshots (b)–(f) are at applied deformation of $u = 5.100$ mm, $u = 5.566$ mm, $u = 5.660$ mm, $u = 5.682$ mm, $u = 5.684$ mm respectively.

temperature-displacement condition, only the hexahedron element is provided with the hybrid formulation (C3D8HT), which is necessary for UYHPER calculation. The tetrahedron element (C3D4T), unfortunately, is not provided with hybrid formulation in ABAQUS and thus cannot be used in this 3D example. The geometry and the 3D finite element mesh of the specimen can be viewed in Fig. 8a.

The deformed configurations of the 3D single edge notch specimen at different time steps are depicted in Fig. 8, which shows the entire crack evolution until the final rupture. Fig. 8a is the geometry (mm) of the specimen with the initial notch of 5 mm width. Fig. 8b shows vividly the large deformation of a hyperelastic material in 3D ($u = 5.100$ mm), up to which the fracture phase field is virtually undeveloped. Fig. 8c shows the deformed configuration of the specimen and the contour of the phase field after an overall deformation of $u = 5.566$ mm, in which state the crack starts to propagate. For an applied deformation of $u = 5.660$ mm the fracture phase field is fully developed in the vicinity of the horizontal notch and a drastic increase in crack growth occurs (Fig. 8d). Fig. 8e–f report the specimen at prescribed boundary displacements of $u = 5.682$ mm, 5.684 mm. The crack is propagating continuously until the hyperelastic material separates into two parts. The visualization contour label of the fracture phase field d (NT11) is set the same as that of Section 3.2 for reference. This 3D example is included in the Supplementary material with the corresponding source code.

Stability problems are frequently encountered during the crack propagation, since the stiffness and stress fall fast in a small number of elements. In simulation, the stress needs to redistribute, and the Newton-Raphson method needs a significant amount of internal iterations to converge, due to the abrupt change in the stiffness of model. In our simulation, we do not encounter many stability problems, due to the robustness of built-in UHYPER subroutine. User subroutine UHYPER is specifically designed for hyperelastic material, which is called at all material calculation points of elements for which the material definition contains user-defined hyperelastic behaviour. However, before the UHYPER implementation method is considered, inspired by Molnar and Gravouil's linear elastic implementation in UEL [26], the User-defined Element subroutine (UEL) method is adopted to implement the calculation of nonlinear FEM (the input and Fortran file is included in the Supplementary material), the simulation is aborted before the crack propagation due to the excessively distorted meshes. Following Navidtehrani et al's linear elastic implementation and hydrogel implementation in UMAT [27,41,42], we also study the User-defined Material (UMAT) method to simulate the NeoHookean model (see the Input and Fortran file for detail in the Supplementary material). However, the calculation processes of these implementations are always interrupted due to the excessively distorted element. Thus, to the best of our knowledge, this proposed UHYPER method is by far the most robust implementation of the phase field simulation for fracture in hyperelastic material.

The framework can be very easily extended to other hyperelastic material models (e.g., Arruda-Boyce model [43]) and hydrogel models under different stimuli, such as temperature and pH [44,45], and coupled with diffusion [46].

4. Numerical fracture examples of hydrogels

In Section 4, we expand the UHYPER implementation from the NeoHookean model to the hydrogel model. Our group has developed a robust UHYPER hydrogel model [37], which has been successfully extended to gels with different stimuli [38,47,48]. By

exploiting the UHYPER hydrogel model, we proposed this UHYPER implementation of a phase field theory to simulate the fracture in the hydrogel. Starting with the 2D case in which we study the single notched gel under different chemical potentials. Then, the 3D single notch specimens with different thicknesses are studied in the section.

4.1. 2D single notched gel under different chemical potential

Our first benchmark test for hydrogel simulation is the single edge notched tensile sample. The geometry of the gel sample is the same as that of Section 3.2 with an initial 20 mm crack length. The bottom side of the rectangular specimen is fixed, while the top side is moved. We have normalized the chemical potential by k_BT. At room temperature, the value k_BT is 4×10^{-21} J and a representative value of k_BT/ν is 40 MPa. The Flory–Rehner free-energy function introduces two dimensionless material parameters: $N\nu$ and χ. In the absence of solvent molecules, the dry network has a shear modulus Nk_BT 0.4 MPa, the same as the shear modulus G in Section 3, which gives $N\nu$ the value of 0.01. The parameter χ is a dimensionless measure of the enthalpy of mixing, with representative values $\chi = 0.1$.

At the initial state, the gel is under the free swelling state with no stress ($T = 0$) and no damage ($d = 0$). Thus Eq. (13) can be rewritten as:

$$N\nu\left(\frac{1}{\lambda_0}-\frac{1}{\lambda_0^3}\right)+\ln\left(1-\frac{1}{\lambda_0^3}\right)+\frac{1}{\lambda_0^3}+\frac{\chi}{\lambda_0^6}=\frac{\mu_0}{k_BT}, \tag{49}$$

where λ_0 is the initial stretch of the gel, and μ_0/k_BT is the dimensionless initial chemical potential.

At the initial state, the water content ϕ can be has a direct relationship with the initial stretch λ_0:

$$\lambda_0 = \frac{1}{\sqrt[3]{1-\phi}}. \tag{50}$$

The water content ϕ of the gel samples varies and has the values ϕ=(90 %, 80 %, 70 %, 60 %, 50 %). Based on Eqs. (49) and (50), the initial stretch λ_0 and chemical potential μ_0/k_BT can be calculated and have the values λ_0=(2.1544, 1.7100, 1.4938, 1.3572, 1.2599) and μ_0/k_BT=(-7.1893×10^{-4}, -1.5296×10^{-2}, -4.3981×10^{-2}, -9.1458×10^{-2}, -1.6521×10^{-1}) respectively (the input file with 90 % water content is included in the Supplementary material). The region around the crack path is refined in order to reach the maximum of $h = 0.1$ mm mesh size, which is 1/10 of the length scale parameter l_c (1 mm). To precisely follow the overall propagation of hydrogel with different water content ϕ, tensile loading is applied by $\Delta u = 2 \times 10^{-3}$ mm for 10,000 steps.

The deformed configurations of the hydrogel specimen at different cracking states are depicted in in Fig. 9 and Fig. 10, which demonstrate the crack evolution until the final rupture. Fig. 9 a, d, g, j, m show that the phase field is developed to some amount around the initial notch tip of the gel specimen with different water content. Fig. 9 b, e, h, k, n represent the propagation of fracture, at which the maximum load is almost reached. After this point the load is drastically decreasing. Fig. 9 c, f, i, l, o depict the subsequent

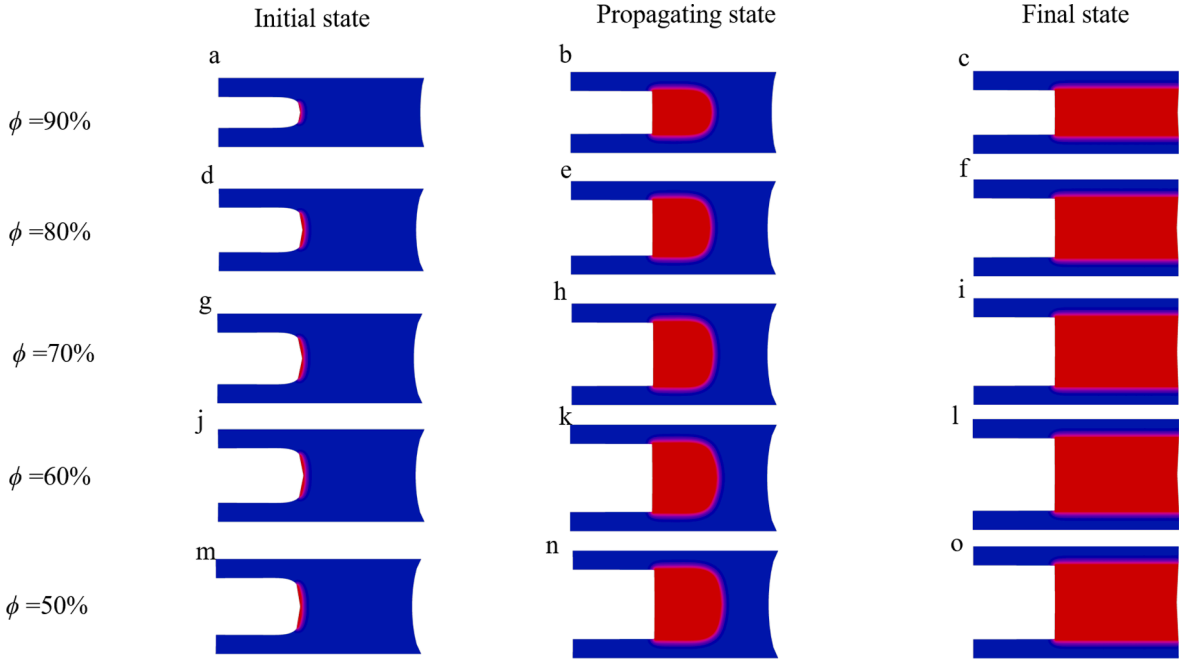

Fig. 9. The snapshots (a)–(o): the crack pattern at the initial, propagating, and final states for hydrogel with 90 %, 80 %, 70 %, 60 %, and 50 % water content (ϕ) respectively. Effective element size of 0.1 mm and length scale of 1 mm.

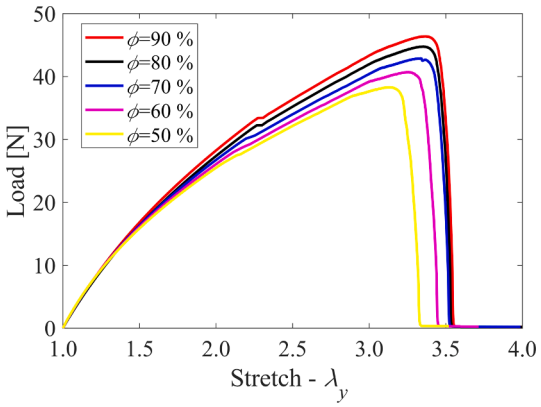

Fig. 10. The load as a function of axial stretch in y direction for single edge notched hydrogel simulations with water content ϕ= (90 %, 80 %, 70 %, 60 %, 50 %) carried out with$N\nu = 0.01$ and$\chi = 0.1$.

propagation of the crack until the body has separated into two parts. The contour plot label of the fracture phase field d is the same as that of Section 3.2.

When comparing the numerical results of hydrogel with different water contentϕ, we observe that the maximum loading force increases as the water content increases. This can be explained by the history variable passed into the governing partial differential equation, the free energy density, Eq. (11), which has a slower increase during the crack propagation as the water content increases. The maximum loading force that is reached until the rapid crack propagation occurs is predicted by the model in all cases in a satisfying way. This validates the capabilities of the presented model for the prediction of fracture in hydrogels.

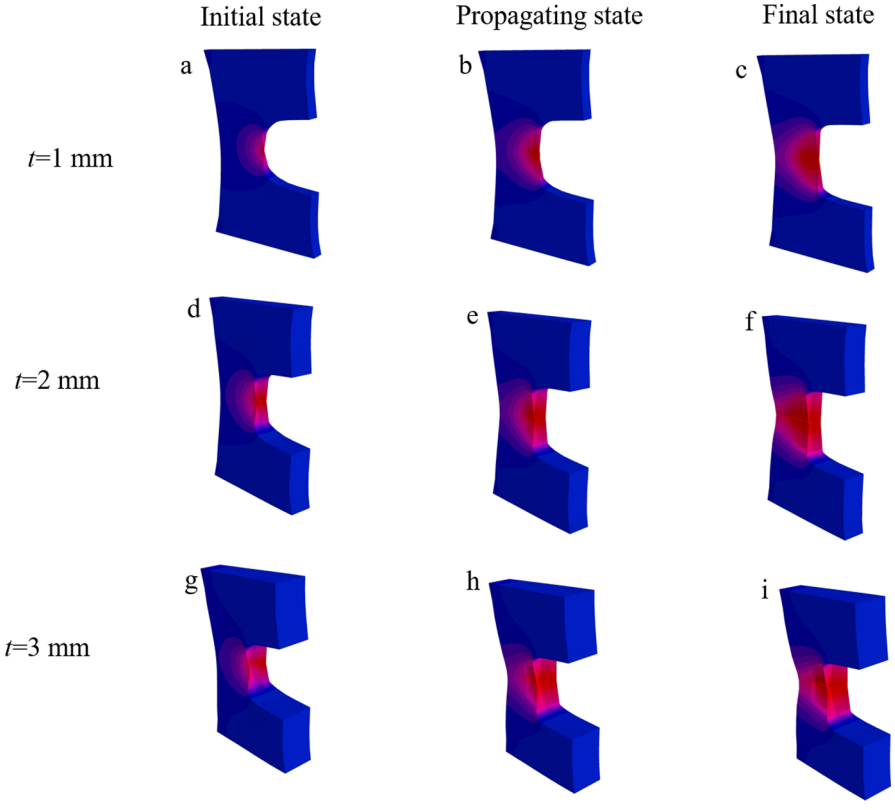

Fig. 11. The snapshots (a)–(i): the crack pattern at the initial, propagating, and final states for hydrogel with the plate thickness $t = 3$ mm, 2 mm, 1 mm respectively. Effective element size of 0.1 mm and length scale of 1 mm.

4.2. 3D single notched plate of hydrogel

Our second benchmark test for hydrogel simulation is the three-dimensional notched plate case, the same as that of Section 3.4. The water content ϕ of the gel samples is 90 % with varying thicknesses of the plate ($t_h = 3$ mm, 2 mm, 1 mm). The mesh size h and the length scale parameter l_c are taken the same as that of Section 4.1.

The deformed configurations of the hydrogel specimen at different cracking states are shown in Figs. 11 and 12, which demonstrate the crack evolution until the final rupture. Fig. 11 a, d, g show the damage field when the crack initiates. Fig. 11 b, e, h represent the propagation of fracture, at which the maximum load is nearly reached. Fig. 11 c, f, i depict the subsequent propagation of the crack until the body has separated into two parts. The contour plots label of the damage field d is the same as that of Section 3.2.

Fig. 12 shows the load deflection curves obtained from the simulation for the three specimen geometries ($t_h = 3$ mm, 2 mm, 1 mm). When comparing the numerical results of hydrogel with different plate thicknesses t_h, it can be roughly concluded that the increase of the thickness t_h results in the maximum stretch of the gel. The maximum loading force is also reached until the rapid crack propagation occurs, which is predicted by the model in all three cases. This validates the capabilities of the presented model for the prediction of 3D fracture in hydrogels.

5. Experimental verification

To verify our purposed model, we first compare the experimental results in the literature with the simulation predictions. Then we conduct the experiment of the fracture of polydimethylsiloxane (PDMS) and hydrogel and compared them with the simulation.

5.1. Rubber fracture study

Hocine et al. have studied the boundary value problems with double edge notch tension rubber specimens to estimate the critical fracture energy [49]. The geometric setup that all the specimens have in common is the same of the example in Section 3.2, depicted in Fig. 7a where all dimensions are given in [mm]. The initial crack length a varies and has the values 20, 24, 28 mm respectively. In our simulation, the effective element size h, the length-scale parameter l_c are the same as that of Section 3.2. The shear modulus of the specimen is set to $G = 0.203$ MPa and the bulk modulus to $K = 1.962$ Mpa, rendering the Poisson's ratio $\nu = 0.45$, the same from Hocine et al. The critical energy release rate is $g_c = 2.67$ N/mm. Fig. 13 shows the load deflection of the experiments and those curves obtained from the simulation for the five specimen geometries. The dots are the load–displacement curves experimentally determined, the curves are the results from the simulations. The geometric setup with the largest initial notch $a = 28$ mm results in the load–displacement curve with the lowest fracture force level. We can conclude that the smaller the initial notch, the higher is the strength of the entire system. When comparing the experimental and the numerical results in Fig. 13, we can observe that the maximum load is reached until the rapid crack propagation occurs in all cases in both experimental and the numerical results. The load–displacement result also agrees with the work of Miehe et al. [40] with the same material parameters.

5.2. PDMS fracture experimental study

Then we conduct the experiment of the fracture of polydimethylsiloxane (PDMS) and compared them with the simulation. SYLGARD 184 silicon elastomer (Dow Corning Corporation) consists of pre-polymer (base) and cross-linker (curing agent) which are mixed with 10:1 mixing ratio (measured by weight). The elastomer components are stirred for approximately 5 min. Since air bubbles are usually generated during stirring, the mixture is placed in a vacuum chamber for up to two hours for degassing. Then the mixture is

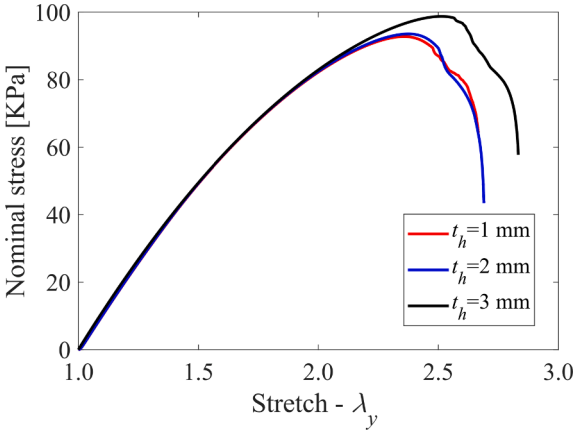

Fig. 12. The nominal stress as a function of axial stretch in y direction for the 3D single edge notched hydrogel plate simulations with plate thicknessses $t_h = 3$ mm, 2 mm, 1 mm carried out with$N\nu = 0.01$ and$\chi = 0.1$.

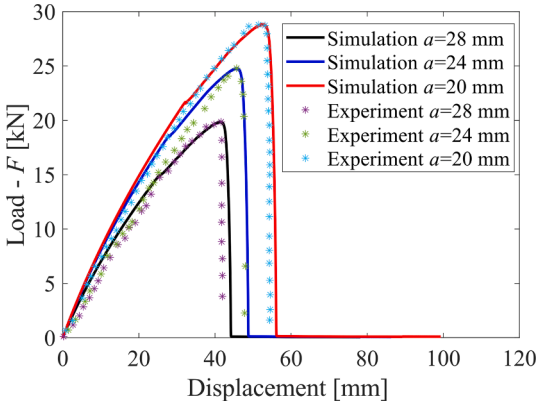

Fig. 13. Comparison of experimental load–displacement result from Hocine et al. [49] with the simulations at chosen material parameters for different initial notches ($l_c = 1$ mm, $G = 0.203$ MPa, $\nu = 0.45$, and $g_c = 2.67$ N/mm) .

moved into the 1 mm thick glass mold. Then the sample is then suspended vertically for 30 min to get rid of any remaining bubbles in the uncured PDMS. Finally, the prepared sample is placed into the oven at 100 °C to cure.

After finishing the curing, the sample is taken out and cut into a rectangle shape by a laser cutting machine. Initial 5 mm edge crack (type I) and 4 mm center crack (type II) are made in the sample as shown in Fig. 14.

Tensile tests of different samples are conducted using SHIMADZU AGS-X loading machine. All the samples are measured at a fixed crosshead velocity of 5 mm/min to assure static loading. The Photron FASTCAM SA-Z high-speed camera is used to record the crack propagation.

We obtain the shear modulus and the bulk modulus of the specimen by the tensile tests ($G = 0.56$ MPa, $K = 6.814$ MPa). In order to capture the crack pattern properly, the mesh is refined where the crack is expected to propagate. In the critical zone an effective element size of $h = 0.1$ mm is chosen. The length-scale parameter applied in the simulations is $l_c = 1$ mm, the same as that of Section 3 and 4. The computations are performed in a staggered method, with the critical fracture energy $g_c = 0.3$ N/mm.

Fig. 15 and Fig. 16 show the crack propagation of type I and II samples and the corresponding simulation snapshots. For side-crack sample, from the simulation snapshots, we can clearly observe the opening of the crack and the propagation of the crack, which is in good agreement with pictures taken by the high-speed camera during experiments. For Type II PDMS sample, due to the imperfection of the cut during the experiment, the initial crack is not exactly in the middle of the specimen. Based on the snapshot taken by the high-speed camera, the center of the crack is located $\sim$ 1 mm to the left, which is the setting of the simulation. This results in that the crack doesn't propagate simultaneously to both sides, but first propagates to the left side and then the right side. The high-speed camera clearly records the crack propagation (Fig. 16). It is observed that the propagation of the central crack can be divided into two parts: first it propagates on one side until the rupture of this side; then it propagates on the other side, until the final rupture. In order to simulate the phenomenon, the center of the crack moves 1 mm to the left during the simulation. From Fig. 16, we can find that simulation of the center-crack propagation is in good agreement with experimental snapshots. The contour plot label of the fracture phase field d is the same as that of Section 3.2.

5.3. PAAM hydrogel experimental study

Finally, to compare the fracture process simulated by our phase field method with experiments, we prepared poly-acrylamide (PAAm) hydrogel samples with pre-cracks and conduct pure shear tests. The pure test was first proposed in Rivlin and Thomas [50] to test fracture of rubber samples and has been recently adopted to characterize gel fracture [51–53]. The undeformed sample is a long thin strip of width, height and thickness with width$\gg$ height and thickness (see Fig. 17a). A long crack of length lies in the middle between the top and bottom boundaries of the strip which are clamped to the loading device. Typically, a uniform vertical displacement is imposed on the top and bottom of the strip. In this study, PAAm hydrogel samples are prepared using the following substances. Acylamide (AAm, Aladdin Industrial Corp., Shanghai, China), N, *N*-methylenebisacrylamide (MBAA, Aladdin Industrial Corp., Shanghai, China), 2-Hydroxy-4′-(2-hydroxyethoxy) − 2-methyl-propiophenone (Irgacure 2959, Aladdin Industrial Corp., Shanghai, China), and water are used as the monomer, crosslinker, light-cure initiator and solvent respectively. AAM:MBAA is 16:0.064(weight ratio). The precursor solution is stirred for 10 min, injected into glass molds (10 mm × 10 mm × 1 mm), and then cured with a UV light for 2 h to form cross-linked polymer networks. The as-prepared PAAm hydrogel sample has a water content of 83 %.

As shown in Fig. 17a, the PAAm hydrogel sample is clamped with the deformable region of 50.0 mm × 10.0 mm and cut to create a pre-crack with a length of 20 mm. A stretch machine (SHIMADZU AGS-X, Shimadzu Corp., Kyoto, Japan) provides a loading rate of 10 mm/min for the tension test. Fig. 17 shows the crack propagation process of the PAAm hydrogel sample. The black dots in the PAAm hydrogel sample are powder for visualization.

We obtain the shear modulus of the hydrogel specimen by the tensile tests ($G = 0.41$ MPa), which gives $N\nu$ the value of 0.0102. The

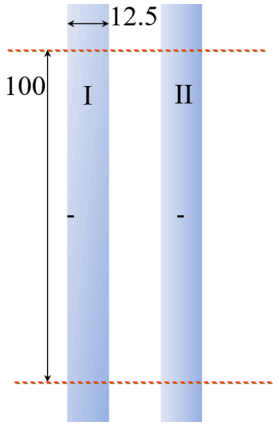

Fig. 14. The geometry of specimens with a configuration of 100 × 12.5 × 1 [mm]. Type I is the sample with 5 mm edge crack; type II is the sample with 4 mm center crack.

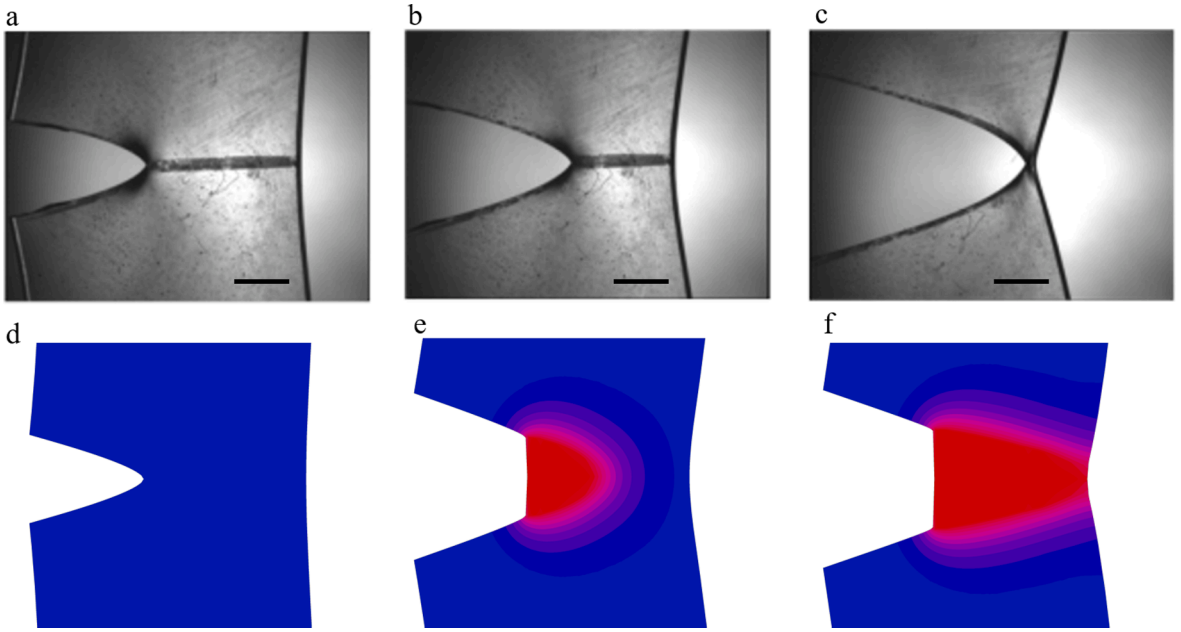

Fig. 15. Crack propagation of type I sample. The snapshots (a)–(c) taken by the high-speed camera are the initial crack, crack propogation, final stage respectively; the snapshots (d)–(f) are the corresponding simulation of (a)–(c). The scale bar is 2 mm.

parameter χ is takes values$\chi = 0.1$. The as-prepared PAAm hydrogel sample has a water content of $\phi = 83$ %, which gives λ_0 and μ_0/k_BT the value of 1.8052 and −0.0095 respectively based on Eq.s (49) and (50). In order to capture the crack pattern properly, the mesh is refined where the crack is expected to propagate. In the critical zone an effective element size of $h = 0.1$ mm is chosen. The length-scale parameter l_c is $= 1$ mm, the same as that of Sections 3 and 4. The computations are performed in a staggered method, with the critical fracture energy $g_c = 0.4$ N/mm.

It is found that the PAAm hydrogel sample undergoes a ductile fracture with significant crack propagation when the stretch reaches 1.39 and ends when the stretch is 1.41. In our 2D phase field model, we can find that simulation of the crack propagation is in good agreement with experimental snapshots. The contour plot label of the fracture phase field d is the same as that of Section 3.2. This qualitative comparison indicates that the phase field model is robust enough to simulate the fracture process of cross-linked hydrogels.

6. Concluding remarks

We have proposed a robust implementation of the phase field fracture method in ABAQUS, which takes advantage of the majority of the in-built features of the commercial software. We built this implementation by utilizing the similarities between the heat transfer model and the phase field model. The proposed implementation is accomplished by combining the hyperelastic user material

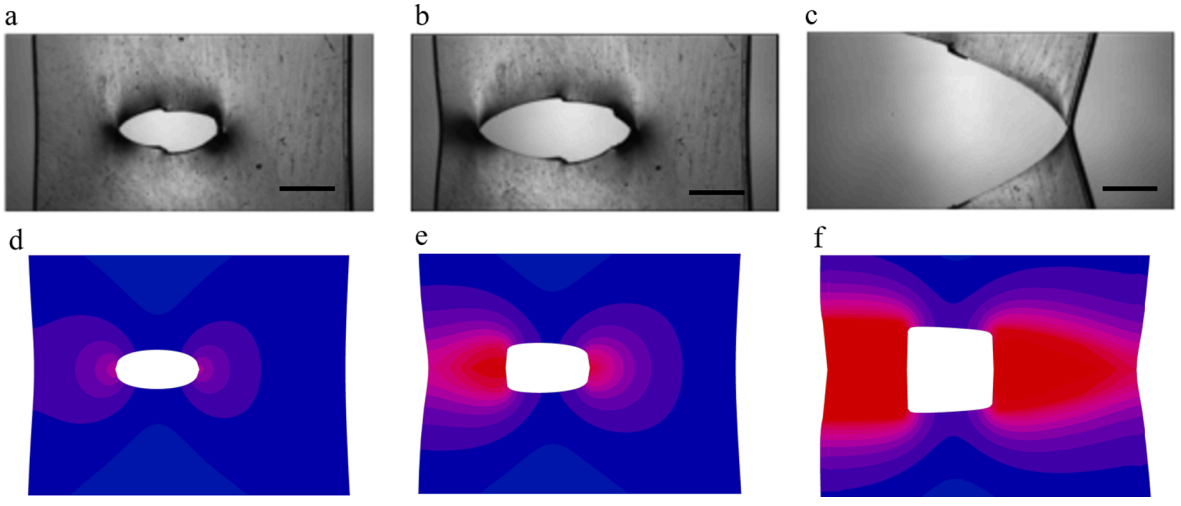

Fig. 16. Crack propagation of type II sample. The snapshots (a)–(c) taken by the high-speed camera are the initial crack, crack propagation, final stage respectively; the snapshots (d) – (f) are the corresponding simulations of (a)–(c). The scale bar is 2 mm.

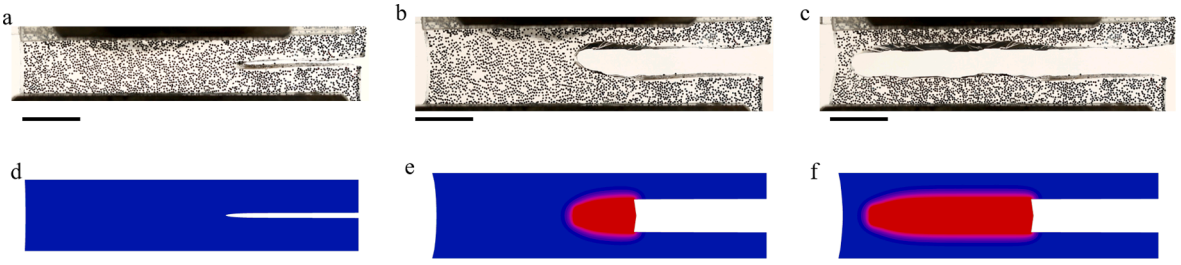

Fig. 17. The crack propagation process of the PAAm hydrogel. (a) Initial sample with a 20 mm pre-crack. (b) The crack propagates significantly when the stretch reaches 1.39. (c) The last snapshot before the fracture occurs when the stretch is 1.41. (d) – (f) are the corresponding simulations of (a) – (c). The scale bar is 10 mm.**Declaration of interests**.

subroutine (UHYPER) and the heat flux subroutine (HETVAL). The code, provided in the Supplementary materials, can be used without changes for both 2D and 3D boundary condition problems. The proposed framework is implemented in both staggered and monolithic solution schemes. Moreover, the framework is general and can accommodate a wide variety of constitutive material models. Specifically, we incorporate the framework with both the NeoHooken constitutive model for the general hyperelastic material and the hydrogel model.

The potential and robustness of the implementation are demonstrated by addressing several 2D and 3D boundary value problems at large deformation. We have examined one element uniaxial tension test, single and double edge notched test for hyperelastic materials. We have also simulated the hydrogel fracture tests, including the modelling of the gel with different water content and thickness. We observe that the staggered implementation appears to be more robust and efficient than the monolithic method, in which the calculation appears divergent after 5000 interactions and a smaller iteration step is required during unstable cracking. We also find that the use of the adaptive meshing method and restart schemes might not lead to efficiency improvements in phase field fracture at large deformation while the automatic stabilization scheme improves the efficiency greatly.

CRediT authorship contribution statement

Shoujing Zheng: Writing – review & editing, Writing – original draft, Validation, Methodology, Investigation, Data curation, Conceptualization. **Rong Huang:** Writing – original draft, Validation, Methodology, Investigation, Data curation, Conceptualization. **Ruijie Lin:** Validation, Methodology, Investigation, Data curation, Conceptualization. **Zishun Liu:** Writing – review & editing, Validation, Supervision, Resources, Project administration, Funding acquisition, Conceptualization.

Declaration of Competing Interest

The authors declare that they have no known competing financial interests or personal relationships that could have appeared to influence the work reported in this paper.

Data availability

Data will be made available on request.

Acknowledgment

The authors are grateful for the support from the National Natural Science Foundation of China through grant number 11820101001 and 12172273.

Appendix A. UHYPER and HETVAL implementation details of the numerical examples

The online Supplemental materials should prove useful to researchers trying to adapt UHYPER's for their own use in other coupled fracture problems. The present section shows a simple example, which can be used to create any model in ABAQUS /Standard with the phase field fracture model. The problem which is going to be solved is just one CPS4T element subjected to a uniaxial tension. This example is shown in the first Supplementary folder (ABAQUS input file and FORTRAN code). Every problem needs two files: an ABAQUS input file (*.inp) and a FORTRAN file (*.for). The FORTRAN file don't need to be changed for the same constitutive model.

In the first section the parts are created. The nodes are given (*Node) and the elements are generated. We use the temperature-displacement element to define the phase field element type (*Element, type = CPS4T). This command creates a plane stress element with four nodes in 2D. The status variables are used to transport information from one step to the next (*Depvar 4), which contains the phase field value and the history variable at each integration point.

The five user-defined material properties for hyperelastic material are defined as follows: shear modulus coefficient C10 ($C10 = G/2$), bulk modulus coefficient D ($D = 2/K$), length scale parameter (l_c), fracture surface energy (g_c), solution flag coefficient (0 for monolithic and 1 for staggered scheme). The eight user-defined material properties for hydrogel are defined as follows: dimensionless modulus coefficient$N\nu$, mixing coefficientχ, initial stretch λ_0 dimensionless chemical potentialμ/k_BT, length scale parameter (l_c), fracture surface energy (g_c), solution flag coefficient, parameterk_BT/ν.

To visualize the results simply open the concerning *.odb file and select the desired state variable in contour plot mode (NT11 for the damage field).

References

[1] Sun J-Y, Zhao X, Illeperuma WRK, Chaudhuri O, Oh KH, Mooney DJ, et al. Highly stretchable and tough hydrogels. Nature 2012;489(7414):133–6.
[2] Wang JQ, Satoh M. A novel reversible thermo-swelling hydrogel. eXPRESS Polym Lett 2010;4(7):450–4.
[3] Yuan X, Nie W-C, Xu C, Wang X-H, Xiao Q, Song F, et al. From Fragility to Flexibility: Construction of Hydrogel Bridges toward a Flexible Multifunctional Free-Standing CaCO3 Film. Adv Funct Mater 2018;28(5):1704956.
[4] Das D, Maiti S, Brahmachari S, Das PK. Refining hydrogelator design: soft materials with improved gelation ability, biocompatibility and matrix for in situ synthesis of specific shaped GNP. Soft Matter 2011;7:7291–303.
[5] Zhao X. Designing toughness and strength for soft materials. PNAS 2017;114(31):8138–40.
[6] Vithani K, Goyanes A, Jannin V, Basit AW, Gaisford S, Boyd BJ. An Overview of 3D Printing Technologies for Soft Materials and Potential Opportunities for Lipid-based Drug Delivery Systems. Pharm Res 2019;36:4.
[7] Stevens MM, Khademhosseini A. Emerging materials for tissue engineering and regenerative medicine: themed issue for Journal of Materials Chemistry and Soft Matter. J Mater Chem 2010;20(40):8729.
[8] Feng G-H, Huang W-L. A self-strain feedback tuning-fork-shaped ionic polymer metal composite clamping actuator with soft matter elasticity-detecting capability for biomedical applications. Mater Sci Eng C-Mater Biol Appl 2014;45:241–9.
[9] Zhang T, Lin S, Yuk H, Zhao X. Predicting fracture energies and crack-tip fields of soft tough materials. Extreme Mech Lett 2015;4:1–8.
[10] Ni X, Yang Z, Li J. Scaling Behavior of Fracture Properties of Tough Adhesive Hydrogels. ACS Macro Lett 2021;10(2):180–5.
[11] Yuk H, Zhang T, Lin S, Parada GA, Zhao X. Tough bonding of hydrogels to diverse non-porous surfaces. Nat Mater. 2016;15:190-+.
[12] Zhang T, Yuk H, Lin S, Parada GA, Zhao X. Tough and tunable adhesion of hydrogels: experiments and models. Acta Mech Sin 2017;33(3):543–54.
[13] Yang Z, Ma Z, Liu S, Li J. Tissue adhesion with tough hydrogels: Experiments and modeling. Mech Mater 2021;157:103800.
[14] Miehe C, Hofacker M, Welschinger F. A phase field model for rate-independent crack propagation: Robust algorithmic implementation based on operator splits. Comput Methods Appl Mech Engng 2010;199(45-48):2765–78.
[15] Miehe C, Welschinger F, Hofacker M. Thermodynamically consistent phase-field models of fracture: Variational principles and multi-field FE implementations. Int J Numer Meth Engng 2010;83(10):1273–311.
[16] Miehe C, Schanzel LM, Ulmer H. Phase field modeling of fracture in multi-physics problems. Part I. Balance of crack surface and failure criteria for brittle crack propagation in thermo-elastic solids. Comput Methods Appl Mech Engng 2015;294:449–85.
[17] Miehe C, Hofacker M, Schanzel LM, Aldakheel F. Phase field modeling of fracture in multi-physics problems. Part II. Coupled brittle-to-ductile failure criteria and crack propagation in thermo-elastic-plastic solids. Comput Methods Appl Mech Engng 2015;294:486–522.
[18] Areias P, Rabczuk T, Msekh MA. Phase-field analysis of finite-strain plates and shells including element subdivision. Comput Methods Appl Mech Engng 2016;312:322–50.
[19] Borden MJ, Hughes TJR, Landis CM, Anvari A, Lee IJ. A phase-field formulation for fracture in ductile materials: Finite defonnation balance law derivation, plastic degradation, and stress triaxiality effects. Comput Methods Appl Mech Engng 2016;312:130–66.
[20] Borden MJ, Hughes TJR, Landis CM, Verhoosel CV. A higher-order phase-field model for brittle fracture: Formulation and analysis within the isogeometric analysis framework. Comput Methods Appl Mech Engng 2014;273:100–18.
[21] Borden MJ, Verhoosel CV, Scott MA, Hughes TJR, Landis CM. A phase-field description of dynamic brittle fracture. Comput Methods Appl Mech Engng 2012;217:77–95.
[22] Heister T, Wheeler MF, Wick T. A primal-dual active set method and predictor-corrector mesh adaptivity for computing fracture propagation using a phase-field approach. Comput Methods Appl Mech Engng 2015;290:466–95.

[23] Liu G, Li Q, Msekh MA, Zuo Z. Abaqus implementation of monolithic and staggered schemes for quasi-static and dynamic fracture phase-field model. Comput Mater Sci 2016;121:35–47.
[24] Fang J, Wu C, Rabczuk T, Wu C, Ma C, Sun G, et al. Phase field fracture in elasto-plastic solids: Abaqus implementation and case studies. Theor Appl Fract Mech 2019;103:102252.
[25] Molnár G, Gravouil A, Seghir R, Réthoré J. An open-source Abaqus implementation of the phase-field method to study the effect of plasticity on the instantaneous fracture toughness in dynamic crack propagation. Comput Methods Appl Mech Engng 2020;365:113004.
[26] Molnar G, Gravouil A. 2D and 3D Abaqus implementation of a robust staggered phase-field solution for modeling brittle fracture. Finite Elem Anal Des 2017;130:27–38.
[27] Navidtehrani Y, Betegón C, Martínez-Pañeda E. A simple and robust Abaqus implementation of the phase field fracture method. Appl Eng Sci 2021;6:100050.
[28] Navidtehrani Y, Betegon C, Martinez-Paneda E. A Unified Abaqus Implementation of the Phase Field Fracture Method Using Only a User Material Subroutine. Materials 2021;14:1913.
[29] Tian F, Tang X, Xu T, Li L. An adaptive edge-based smoothed finite element method (ES-FEM) for phase-field modeling of fractures at large deformations. Comput Methods Appl Mech Engng 2020;372:113376.
[30] Peng F, Huang W, Zhang Z-Q, Fu Guo T, Ma YE. Phase field simulation for fracture behavior of hyperelastic material at large deformation based on edge-based smoothed finite element method. Eng Fract Mech 2020;238:107233.
[31] Loew PJ, Peters B, Beex LAA. Rate-dependent phase-field damage modeling of rubber and its experimental parameter identification. J Mech Phys Solids 2019;127:266–94.
[32] Mandal TK, Gupta A, Nguyen VP, Chowdhury R, Vaucorbeil Ad. A length scale insensitive phase field model for brittle fracture of hyperelastic solids. Eng Fract Mech 2020;236:107196.
[33] Mao YW, Anand L. A theory for fracture of polymeric gels. J Mech Phys Solids 2018;115:30–53.
[34] Boger L, Keip MA, Miehe C. Minimization and saddle-point principles for the phase-field modeling of fracture in hydrogels. Comput Mater Sci 2017;138:474–85.
[35] Gürses E, Miehe C. A computational framework of three-dimensional configurational-force-driven brittle crack propagation. Comput Methods Appl Mech Engng 2009;198(15-16):1413–28.
[36] Tian FC, Zeng J, Tang XL, Xu TY, Li LB. A dynamic phase field model with no attenuation of wave speed for rapid fracture instability in hyperelastic materials. Int J Solids Struct 2020;202:685–98.
[37] Hong W, Liu Z, Suo Z. Inhomogeneous swelling of a gel in equilibrium with a solvent and mechanical load. Int J Solids Struct 2009;46(17):3282–9.
[38] Ding Z, Liu Z, Hu J, Swaddiwudhipong S, Yang Z. Inhomogeneous large deformation study of temperature-sensitive hydrogel. Int J Solids Struct 2013;50(16-17):2610–9.
[39] Toh W, Liu ZS, Ng TY, Hong W. Inhomogeneous large deformation kinetics of polymeric gels. Int J Appl Mech 2013;05(01):1350001.
[40] Miehe C, Schaenzel L-M. Phase field modeling of fracture in rubbery polymers. Part I: Finite elasticity coupled with brittle failure. J Mech Phys Solids 2014;65:93–113.
[41] Kang MK, Huang R. A Variational Approach and Finite Element Implementation for Swelling of Polymeric Hydrogels Under Geometric Constraints. J Appl Mech-Trans Asme 2010:77.
[42] Ilseng A, Prot V, Skallerud BH, Stokke BT. Buckling initiation in layered hydrogels during transient swelling. J Mech Phys Solids 2019;128:219–38.
[43] Arruda EM, Boyce MC. A three-dimensional constitutive model for the large stretch behavior of rubber elastic materials. J Mech Phys Solids 1993;41(2):389–412.
[44] Cai S, Suo Z. Mechanics and chemical thermodynamics of phase transition in temperature-sensitive hydrogels. J Mech Phys Solids 2011;59(11):2259–78.
[45] Toh W, Ng TY, Liu Z, Hu J. Deformation kinetics of pH-sensitive hydrogels. Polym Int 2014;63(9):1578–83.
[46] Jonášová EP, Stokke BT, Prot V. Interrelation between swelling, mechanical constraints and reaction-diffusion processes in molecular responsive hydrogels. Soft Matter 2022;18(7):1510–24.
[47] Marcombe R, Cai S, Hong W, Zhao X, Lapusta Y, Suo Z. A theory of constrained swelling of a pH-sensitive hydrogel. Soft Matter 2010;6:784–93.
[48] Zheng S, Liu Z. Constitutive model of salt concentration-sensitive hydrogel. Mech Mater 2019;136:103092.
[49] Hocine NA, Abdelaziz MN, Imad A. Fracture problems of rubbers: J-integral estimation based upon eta factors and an investigation on the strain energy density distribution as a local criterion. Int J Fract 2002;117:1–23.
[50] Rivlin RS, Thomas AG. Rupture of rubber.I. characteristic energy for tearing. J Polym Sci 1953;10:291–318.
[51] Long R, Hui C-Y. Fracture toughness of hydrogels: measurement and interpretation. Soft Matter 2016;12(39):8069–86.
[52] Zhang W, Hu J, Tang J, Wang Z, Wang J, Lu T, et al. Fracture Toughness and Fatigue Threshold of Tough Hydrogels. ACS Macro Lett 2019;8(1):17–23.
[53] Tang JD, Li JY, Vlassak JJ, Suo ZG. Fatigue fracture of hydrogels. Extreme Mech Lett 2017;10:24–31.